ACS OMEGA

http://pubs.acs.org/journal/acsodf

Article

Effect of pH on the Catalytic Degradation of Rhodamine B by Synthesized CDs/g-C_3N_4/Cu_xO Composites

Yulian Guo, Chunsun Zhou, Lijuan Fang, Zhongda Liu, Wen Li, and Miao Yang*

Cite This: *ACS Omega* 2021, 6, 8119–8130

Read Online

ACCESS | Metrics & More | Article Recommendations | Supporting Information

ABSTRACT: The narrow pH range of Fenton oxidation restricts its applicability in water pollution treatment. In this work, a CDs/g-C_3N_4/Cu_xO composite was synthesized via a stepwise thermal polymerization method using melamine, citric acid, and Cu_2O. Adding H_2O_2 to form a heterogeneous Fenton system can degrade Rhodamine B (Rh B) under dark conditions. The synthesized composite was characterized by Fourier transform infrared (FT-IR) spectroscopy, X-ray diffraction (XRD), transmission electron microscopy (TEM), X-ray photoelectron spectroscopy (XPS), and N_2 adsorption/desorption isotherms. The results showed that CDs, Cu_2O, and CuO were successfully loaded on the surface of g-C_3N_4. By evaluating the catalytic activity on Rh B degradation in the presence of H_2O_2, the optimal contents of citric acid and Cu_2O were 3 and 2.8%, respectively. In contrast to a typical Fenton reaction, which is favored in acidic conditions, the catalytic degradation of Rh B showed a strong pH-dependent relation when the pH is raised from 3 to 11, with the removal from 45 to 96%. Moreover, the recyclability of the composite was evaluated by the removal ratio of Rhodamine B (Rh B) after each cycle. Interestingly, recyclability is also favored in alkaline conditions and shows the best performance at pH 10, with the removal ratio of Rh B kept at 95% even after eight cycles. Through free radical trapping experiments and electron spin resonance (ESR) analysis, the hydroxyl radical ($^{\bullet}OH$) and the superoxide radical ($^{\bullet}O_2^-$) were identified as the main reactive species. Overall, a mechanism is proposed, explaining that the higher catalytic performance in the basic solution is due to the dominating surface reaction and favored in alkaline conditions.

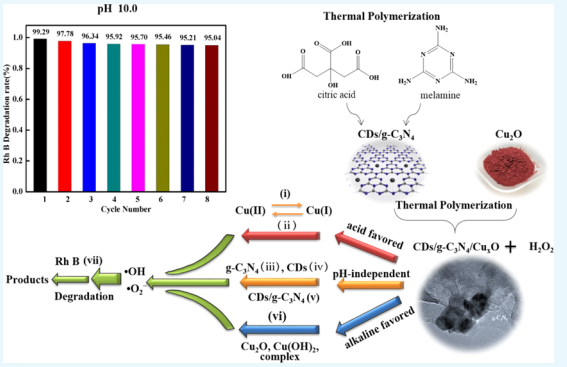

1. INTRODUCTION

Organic pollutants produced by the dye industry are harmful to the environment and human beings due to their high toxicity, persistence, and poor biodegradability.[1,2] The key to advanced oxidation processes (AOPs) is the in situ-produced hydroxyl radical ($^{\bullet}OH$) with relatively high reactivity and nonselectivity for different organic pollutants.[3,4] As one of the most efficient treatments for such organic pollutants, an AOP can mineralize almost all organic pollutants, which can be completely degraded into water, carbon dioxide, and some easily degradable inorganic ions in wastewater without causing secondary pollution.[5−7] Like a typical AOP, a Fenton reaction can produce more number of $^{\bullet}OH$ when the ferrous ions react with hydrogen peroxide (H_2O_2).[8] Some disadvantages of the Fenton reaction are a narrow pH range (pH < 4), the formation of iron sludge, and the high cost of catalyst recovery.[9−11]

Graphitic carbon nitride (g-C_3N_4), a nonmetallic semiconductor, has a wide range of applications due to the narrow band gap (2.7 eV), low cost, nontoxicity, good chemical stability, and superior resistance to acids and alkalis.[12,13] However, some shortcomings, such as a high photoexciting electron−hole recombination, low specific surface area, and low utilization rate,[14,15] limit the application of g-C_3N_4 in the field of photocatalysts. Therefore, many strategies, such as changing the morphology,[16] nonmetal or metal and metal oxide loading,[17−19] construction of heterojunctions, etc.,[20,21] have been employed to improve its photocatalytic performance. Among these strategies, the use of carbon nanodots (CDs) to modify g-C_3N_4 not only increased the specific surface area of pure g-C_3N_4 but also improved its photocatalytic activity and promoted photocatalytic H_2 production.[22]

On this basis, several studies have been conducted by introducing a third compound (e.g., TiO_2, Ag_3PO_4, Ag nanoparticles, etc.) into CDs/g-C_3N_4 to further improve the photocatalytic performance on H_2 production or pollutant degradation.[23−25] Besides improving the photocatalytic performance, the CDs/g-C_3N_4 composite may also act as a Fenton-like catalyst and catalyze the decomposition of H_2O_2 to form $^{\bullet}OH$ in the light-shielding condition according to its intrinsic

Received: December 4, 2020
Accepted: March 3, 2021
Published: March 15, 2021

https://dx.doi.org/10.1021/acsomega.0c05915
ACS Omega 2021, 6, 8119−8130

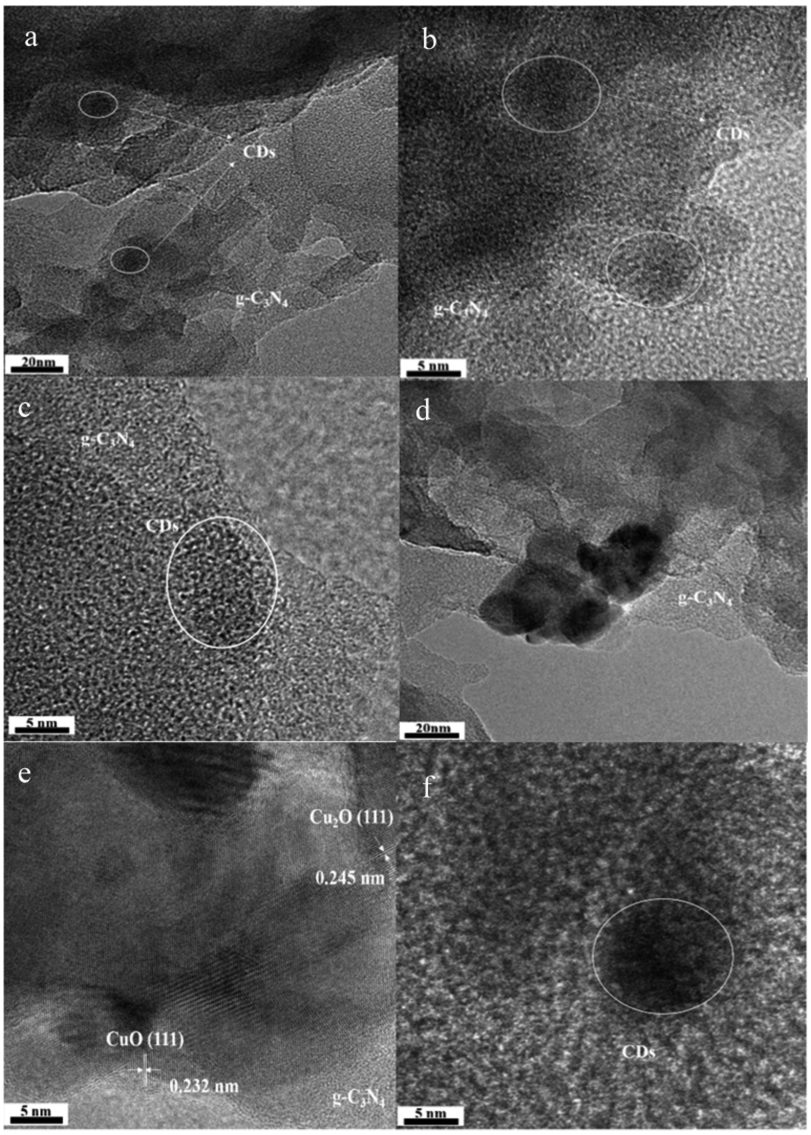

Figure 1. TEM and HRTEM images of CD_3/g-C_3N_4 (a−c) and CDs/g-C_3N_4/Cu_xO (d−f).

property, which has been used to remove organic pollutants.[26] Recent studies have shown that in some pollutants, the introduction of a metal oxide into the CDs/g-C_3N_4 matrix may improve the degradation efficiency, such as loading ZnO on the surface of CDs/g-C_3N_4 to prepare a CDs/g-C_3N_4/ZnO nanocomposite for tetracycline total degradation.[27]

Similar to the redox properties of iron, copper can undergo a Fenton-like system with H_2O_2 to achieve mutual conversion between Cu^+ and Cu^{2+} and produce $^{\bullet}OH$, as shown in eqs 1 and 2.[28,29] It should be noted that eq 2 is a rate-limiting step and Cu^{2+} can be from a copper complex $[Cu(H_2O)_6]^+$ at a neutral pH, which can be used in the $Cu^{2+}/Cu^+/H_2O_2$ Fenton-like system.[30] Cu^+/Cu^{2+} has limited applicability due to the narrow range of pH and the extreme volatility of Cu^+. Therefore, to expand the application of CDs/g-C_3N_4 and overcome some limitations of the Fenton system and the Cu^+/Cu^{2+} Fenton-like system, this study chose to load Cu_2O on CDs/g-C_3N_4 and form a Fenton-like system for the degradation of Rh B in the reaction.

$$Cu^+ + H_2O_2 \rightarrow Cu^{2+} + {}^{\bullet}OH + OH^- \quad k = 1.0 \times 10^4\ M^{-1}\ s^{-1} \tag{1}$$

$$Cu^{2+} + H_2O_2 \rightarrow Cu^+ + {}^{\bullet}O_2H + OH^- \quad k = 4.6 \times 10^2\ M^{-1}\ s^{-1} \tag{2}$$

In this study, a more promising strategy is proposed to fix Cu_2O on CDs/g-C_3N_4 by thermal polymerization, in which CDs/g-C_3N_4/Cu_xO composites are obtained that can initiate a Fenton-like reaction in the presence of H_2O_2 to generate active free radicals that are used for the degradation of organic pollution. The prepared composites were characterized by FT-IR, XRD, TEM, XPS, and BET techniques. The optimal synthesis and experiment conditions, including CDs content, Cu_2O content, H_2O_2 concentration, solution ion reaction, and influence of different pH values, were explored. Also, to further explore the reasons for the differences in the changes at different pH conditions, the changes in the dissolved oxygen, total copper content, and the stability of composites at different pH values were studied. Besides, reactive oxygen species (ROS) were investigated by ESR analysis and free radical capture experiments. Based on the above results, the degradation mechanism of Rh B was outlined in the presence of H_2O_2 with the CDs/g-C_3N_4/Cu_xO composite in a wide range of pH conditions.

https://dx.doi.org/10.1021/acsomega.0c05915
ACS Omega 2021, 6, 8119−8130

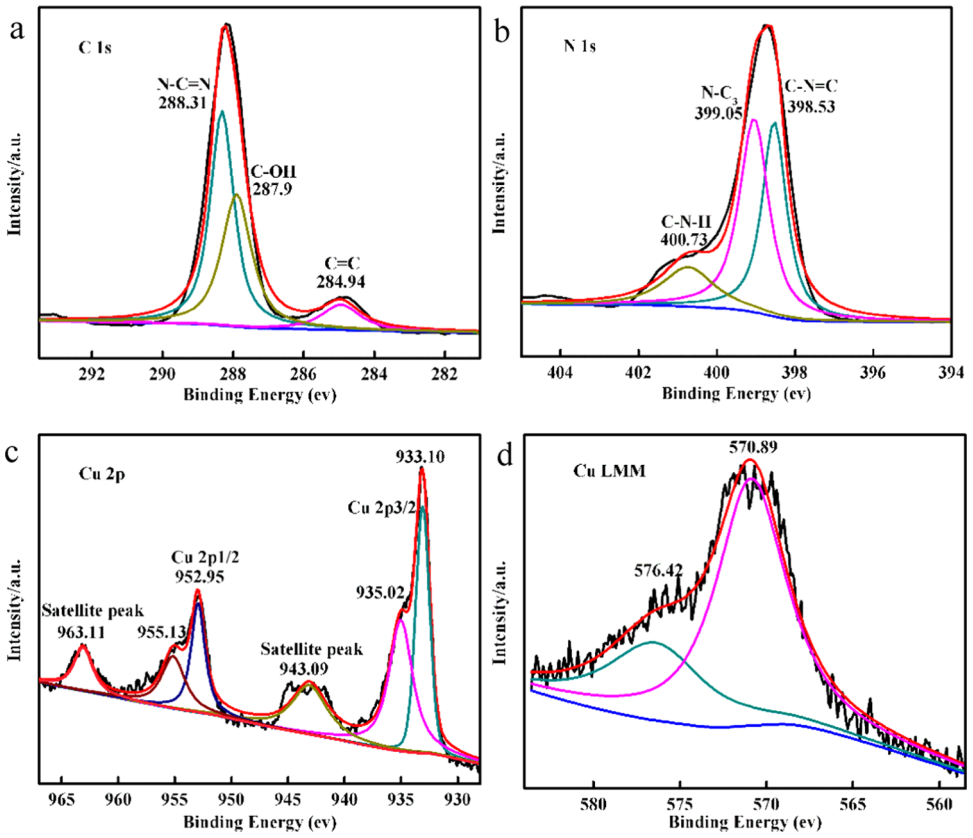

Figure 2. High-resolution (a) C 1s, (b) N 1s, (c) Cu 2p, and (d) Cu LMM spectra of the CDs/g-C_3N_4/Cu_xO composite.

2. RESULTS AND DISCUSSION

2.1. Characterization of Catalysts. *2.1.1. FT-IR.* The as-prepared composites, labeled as g-C_3N_4, CD_3/g-C_3N_4, and CDs/g-C_3N_4/Cu_xO, were investigated to distinguish the functional groups via the FT-IR spectrum. As presented in Figure S1, the characteristic peaks of g-C_3N_4 were observed at 1200−1645 cm^{-1}, corresponding to the stretching vibration modes of CN-bond heterocycles (C═N and C−N groups).[31] The appearance of the absorption peak at 810 cm^{-1} was allocated to the normal vibration of the tris(3′,5′-dimethylpyrazol-1-yl)-*s*-triazine structure.[32] The aforementioned absorption peaks could be characterized as g-C_3N_4, similar to a previous study.[33] Further, a broadband emerged approximately at 3200 cm^{-1}, which can be allocated to the stretching vibration modes of NH and NH_2 group.[34] For CD_3/g-C_3N_4 and CDs/g-C_3N_4/Cu_xO, similar peaks were present, showing that the skeletal structure of g-C_3N_4 was not damaged in these composites. With Cu_2O doped into CDs/g-C_3N_4/Cu_xO, the corresponding peak of the stretching vibration of the Cu−O bond of Cu_2O and CuO was not detected in FT-IR, implying that the corresponding copper-based functional groups were not formed by thermal polymerization of the synthesized composites.[35,36]

2.1.2. XRD. The crystal structures of Cu_2O, g-C_3N_4, CD_3/g-C_3N_4, and CDs/g-C_3N_4/Cu_xO were acquired via XRD patterns, as shown in Figure S2. For g-C_3N_4, the weak peak close to 13.0° can be indexed to (100) diffraction planes, corresponding to the in-planar structural packing motif of tri-*s*-triazine units. In addition, the strong diffraction peak at 27.5° corresponding to the typical (002) plane was due to the interlayer accumulation of the conjugated aromatic system.[37] Besides the characteristic peaks of g-C_3N_4, with the loading of CDs, the sharp peak of CDs could be detected at 25.25°.[38] After doping with Cu_2O, the characteristic peaks of g-C_3N_4 appeared similar, but three diffraction peaks were observed at 36°, 38°, and 61.5° in CDs/g-C_3N_4/Cu_xO composite, which were in good agreement with the crystalline structure of CuO indexed with the standard $(11\bar{1})$ plane, the (111) plane, and corresponding to the (220) plane of the Cu_2O phase,[39,40] respectively. However, compared to g-C_3N_4 and CD_3/g-C_3N_4, the (100) plane of the diffraction peaks weakened noticeably, the peak corresponding to the (002) plane shifted slightly, and no diffraction peak arose from the CDs in the CDs/g-C_3N_4/Cu_xO composite as Cu_2O addition may affect the thermal condensation of melamine, resulting in lower crystallinity of the (100) and (002) crystal planes. Moreover, the invisible diffraction peak of CDs may be due to the relatively low diffraction intensity in the composite.[38] Therefore, the XRD spectral patterns revealed the coexistence of CuO and Cu_2O in the CDs/g-C_3N_4/Cu_xO composite.

2.1.3. TEM. The morphology and microstructures of CD_3/g-C_3N_4 and CDs/g-C_3N_4/Cu_xO samples were observed by TEM and HRTEM. Figure 1a−c shows that the appearance of the CDs is unevenly embedded in the g-C_3N_4 matrix (white circles), with a diameter of 10−20 nm. This observation was in concordance with the findings of a previous study.[41,42] It indicates that CD_3/g-C_3N_4 was successfully prepared by the thermal polymerization method. Figure 1d shows the TEM images of the CDs/g-C_3N_4/Cu_xO composite and some particles (20−50 nm) fixed on the two-dimensional lamellar structures of g-C_3N_4. As shown by the corresponding HRTEM image in Figure 1e, lattice fringes with interlayer distance were measured to be 0.245 and 0.232 nm, which correspond to the (111) plane of Cu_2O and the (111) plane of CuO.[43,44] XRD results showed Cu_2O and CuO in the CDs/g-C_3N_4/Cu_xO. CDs particles were

https://dx.doi.org/10.1021/acsomega.0c05915
ACS Omega 2021, 6, 8119−8130

found on the surface of the CDs/g-C_3N_4/Cu_xO composite with the same diameter as CDs in CD_3/g-C_3N_4 (Figure 1c,f). A comparison between the TEM and HRTEM of CD_3/g-C_3N_4 and CDs/g-C_3N_4/Cu_xO established that CDs and Cu_2O are successfully loaded on the CDs/g-C_3N_4/Cu_xO surface.

2.1.4. XPS. The elemental and surface chemical states of the CDs/g-C_3N_4/Cu_xO composite were investigated via XPS spectral analysis. Only C, N, O, and Cu were present in the composite, and the atomic content ratios were 41.64, 52.28, 3.98, and 2.1%, respectively (Figure S3). Compared with the standard XPS binding energy table, the binding energy peaks of the four elements get slightly shifted toward the higher values.[19]

The results are shown in Figure 2 and Table S1. Figure 2a shows the high-resolution XPS spectrum of C 1s with peaks at 284.94 and 288.31 eV allocated to C−C and N−C═N, respectively. The peak at 287.90 eV was identified as C−OH, indicating the successful loading of CDs on the CDs/g-C_3N_4/Cu_xO composite.[32] The N 1s spectrum displayed in Figure 2b mainly shows three peaks at 398.53, 399.05, and 400.73 eV, which are located at the triazine rings (C−N═C), the sp^3-hybridized nitrogen (N−C_3), and amino groups (C−N−H),[34] respectively. This indicates that the structure of g-C_3N_4 is not completely altered by the addition of CDs and Cu_2O. For the O 1s spectrum (Figure S4), it contains three peaks, corresponding to 530.57 eV (O═C), 532.04 eV (C−OH), and 533.21 eV (adsorbed water).[32] Figure 2c displays that there are six characteristic peaks in Cu 2p; the binding energies at 933.10 and 952.95 eV were assigned to Cu $2p_{3/2}$ and Cu $2p_{1/2}$ of Cu^+ and those at 935.02 and 955.13 eV were identified as Cu $2p_{3/2}$ and Cu $2p_{1/2}$ of Cu^{2+},[45,46] respectively. The deconvoluted peaks at 943.09 and 963.11 eV, derived from the satellite peaks of Cu^{2+}, established the existence of Cu^{2+} in the composite.[45]

Since the binding energies of Cu^+ and Cu^0 are very close, they are hard to distinguish unless the Cu LMM peak is observed (Figure 2d). The Cu LMM peaks of the composite were observed at 570.89 and 576.42 eV, which was in accordance with the presence of Cu^+.[36] To conclude, the Cu 2p and Cu LMM peaks showed the existence of both Cu^+ and Cu^{2+} ions in the CDs/g-C_3N_4/Cu_xO composite, showing conformity with the results of XRD and TEM. These findings show the successful synthesis of the CDs/g-C_3N_4/Cu_xO composite.

2.1.5. N_2 Adsorption/Desorption Isotherms. The specific surface area and pore-size distribution curves of as-prepared g-C_3N_4, CD_3/g-C_3N_4, and CDs/g-C_3N_4/Cu_xO samples were analyzed by BET. As presented in Figure S5, g-C_3N_4, CD_3/g-C_3N_4, and CDs/g-C_3N_4/Cu_xO exhibit a typical type IV isotherm with a clear H3 hysteresis loop, suggesting the presence of a mesoporous structure with 2−8 nm pore size.[47] The specific surface areas calculated using the BET method were 12.0 ± 0.7, 21.5 ± 1.2, and 90.3 ± 0.5 $m^2 g^{-1}$ for g-C_3N_4, CD_3/g-C_3N_4, and CDs/g-C_3N_4/Cu_xO, respectively, indicating that the mixing with CDs and Cu_2O increases the specific surface area of the g-C_3N_4. The specific surface areas of CDs/g-C_3N_4/Cu_xO were 7.53 times and 4.2 times that of pure g-C_3N_4 and CD_3/g-C_3N_4, respectively. This suggests that the addition of CDs and Cu_2O increases the specific surface area of the CDs/g-C_3N_4/Cu_xO composite and the contact area of the reactant and provides more active sites.

2.2. Evaluation of the Catalytic Performance of CDs/g-C_3N_4/Cu_xO Composites. *2.2.1. Content of CDs.* To determine the optimal content of CDs in the CDs/g-C_3N_4/Cu_xO composite, the catalytic performance on the removal of Rh B in the presence of H_2O_2 and several CD_y/g-C_3N_4 composites with varied contents (1−6%) of CDs was compared. As demonstrated in Figure 3, only 22% of Rh B was removed in

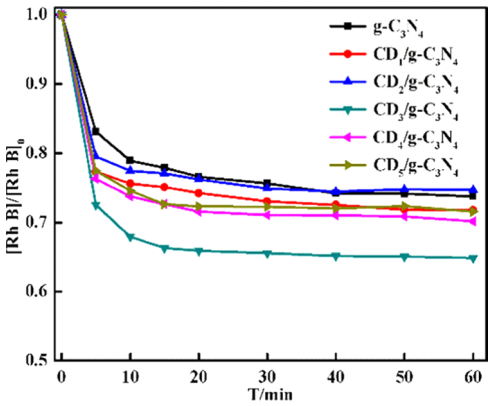

Figure 3. $[Rh B]/[Rh B]_0$ as a function of time in the presence of 5 g/L CD_y/g-C_3N_4 (y = 0−5) with the initial concentration of $[H_2O_2]_0$ = 5 mM, $[Rh B]_0$ = 0.064 mM, and V = 100 mL.

60 min with pure g-C_3N_4, although the removal rate increased dramatically by raising the content of CDs, reaching its maximum when the CD content was 3. The increase in the removal rate could be ascribed to the fact that the higher amount of CDs might aggregate to form clusters and affect the progress of surface reactions.[48] Therefore, the content of optimal CDs was confirmed as y = 3, and CD_3/g-C_3N_4 was selected as the typical composite for further synthesis of CDs/g-C_3N_4/Cu_xO composites.

2.2.2. Effect of Cu_2O Content. The effect of Cu_2O content was studied by evaluating the removal rates of Rh B with CD_3/g-C_3N_4/Cu_xO composites marked as C1−C6 in the presence of H_2O_2. The removal of Rh B was remarkably improved by adding Cu_2O before and after the injection of H_2O_2 (Figure 4a), suggesting that the addition of Cu_2O improves both the adsorption and catalytic performance of the composite. However, the final removal ratio of Rh B was not linearly related to the content of Cu_2O. To be specific, the highest ratio for the adsorption phase and the catalytic degradation phase, during the whole process, responded to C1 and C2, respectively. The H_2O_2 concentration was also monitored (Figure 4b). The results showed that the decomposition of H_2O_2 was also enhanced by raising the amount of Cu_2O, reaching the highest rate at C4. Notably, at C2, Rh B was degraded completely, with only 73.3% of H_2O_2 consumed and exhibited the highest utilization rate, as shown by eq 4. Therefore, the C2 composite was selected for further exploration in subsequent experiments. (C2 was taken as the optimal catalyst for property study. The CDs/g-C_3N_4/Cu_xO composite in the following text refers to C2 unless otherwise stated.)

2.2.3. Effect of H_2O_2 concentration. H_2O_2, as a precursor of $^{\bullet}OH$, was employed to induce Rh B degradation in the presence of the CDs/g-C_3N_4/Cu_xO composite after the system reached the adsorption/desorption equilibrium. To evaluate the effect of H_2O_2, different concentrations of H_2O_2 were added. When the H_2O_2 concentration increased from 1 to 10 mM, the degradation rate of Rh B also increased (Figure S6). The degradation rate and utilization of Rh B (calculated from eq 4) with different concentrations of H_2O_2 are compared in Table S2 (t = 60 min). The higher concentrations of H_2O_2 induced a higher degradation ratio of Rh B. However, the general trend of the utilization rate of H_2O_2 decreased with an increase in the

https://dx.doi.org/10.1021/acsomega.0c05915
ACS Omega 2021, 6, 8119−8130

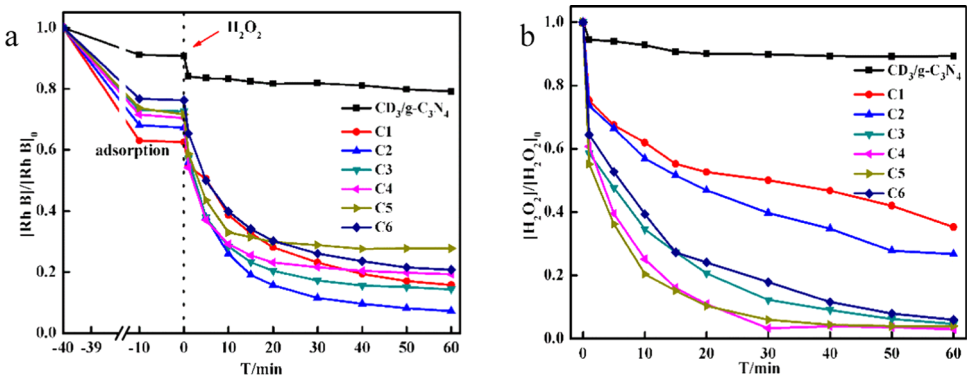

Figure 4. (a) $[Rh\ B]/[Rh\ B]_0$ and (b) $[H_2O_2]/[H_2O_2]_0$ as a function of time in the presence of 2 g/L from C1 to C6 with an initial concentration of $[H_2O_2]_0$ = 5 mM, $[Rh\ B]_0$ = 0.064 mM, and V = 100 mL.

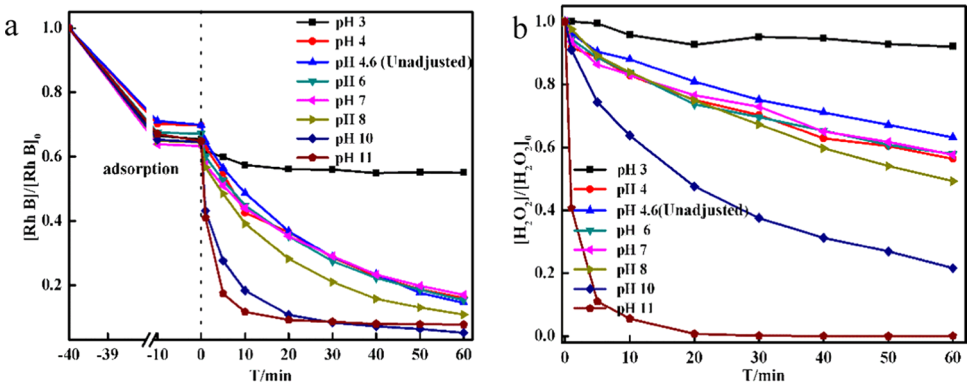

Figure 5. (a) $[Rh\ B]/[Rh\ B]_0$ as a function of time in the presence of 2 g/L CDs/g-C_3N_4/Cu_xO composite at different pH values with the initial concentration of $[H_2O_2]_0$ = 5 mM, $[Rh\ B]_0$ = 0.064 mM, and V = 100 mL. (b) Amount of H_2O_2 consumed by the catalysts in the degradation of Rh B at different pH values.

concentration of H_2O_2 as a very high H_2O_2 concentration was more prone to H_2O_2 decomposition, suggesting that more H_2O_2 concentration could lead to higher production of $^{\bullet}OH$ and that in the side reaction H_2O_2 could be consumed by the formed $^{\bullet}OH$.[49,50] Thus, the H_2O_2 at 5 mM utilization rate was relatively high, and the degradation rate of Rh B was also in the middle. Therefore, considering its degradation rate and utilization together, the optimal concentration of H_2O_2 was selected as 5 mM in other experiments.

2.2.4. Effect of Solution Reaction. To verify the potential homogeneous reaction in the system, a similar experiment was conducted by taking several samples at selected time points, filtering separately, and placing them together to observe the time-resolved concentration of Rh B in the filtrate.[51] The results are summarized in Figure S7a. In contrast to the original heterogeneous reaction, only a slight decrease was observed in all filtrates, indicating a weaker solution reaction as compared to the surface reaction. The concentrations of Rh B and H_2O_2 in the filtrates were monitored from 1 min to several days. Figure S7b shows that Rh B was decomposed completely although at a much lower rate than that of the original heterogeneous system. Therefore, in subsequent experiments, the solution reaction was insignificant.

2.2.5. Effect of pH. 2.2.5.1. Degradation of Rh B and Decomposition of H_2O_2 under Different pH Conditions. The strict pH limitation (pH < 4) is a major disadvantage of various homogeneous Fenton reactions, preventing its application in neutral and alkaline conditions. Therefore, the study of the pH effect in the present system is very important. In the current study, several experiments were conducted by varying the solution pH from 3 to 11 to evaluate the pH effect on the degradation of Rh B and decomposition of H_2O_2. Initially, the Rh B solution was adjusted to different pH conditions and was scanned with an ultraviolet−visible spectrophotometer (Figure S8) to nullify the effect of pH on the maximum absorption peak. It was observed that the maximum absorption peak of Rh B can be maintained at 555 nm with the given pH ranges.

To further explore the effect of pH on the Fenton-like reaction and to compare the catalytic degradation of Rh B with CDs/g-C_3N_4/Cu_xO composites, several different pH conditions were selected. The pH change showed a negligible effect on the adsorption phase (Figure 5a), while during the catalytic degradation phase, the degradation rate of Rh B exhibited a highly basic-favored trend. At pH 10 and 11, the removal rate was significantly higher than that at pH 3. H_2O_2 concentration in the catalytic degradation phase was also monitored (Figure 5b). Despite the similar degradation rate of Rh B at pH 10 and 11 (Figure 5a), the decomposition rate of H_2O_2 was much lower at pH 10 than that at pH 11. As discussed in the previous section, pH 10 showed better utilization efficiency. Therefore, the CDs/g-C_3N_4/Cu_xO composite can be widely used in the application range of pH.

2.2.5.2. Dissolved Oxygen Changes in Solution. To further understand how the decomposition of H_2O_2 is affected by the change in pH since the decomposition of H_2O_2 results in H_2O and O_2, the dissolved oxygen could be used as a probe to study the effect of pH.[52] Figure 6 depicts a similar trend in the concentration of Dissolved Oxygen (DO), reaches a maximum

https://dx.doi.org/10.1021/acsomega.0c05915
ACS Omega 2021, 6, 8119−8130

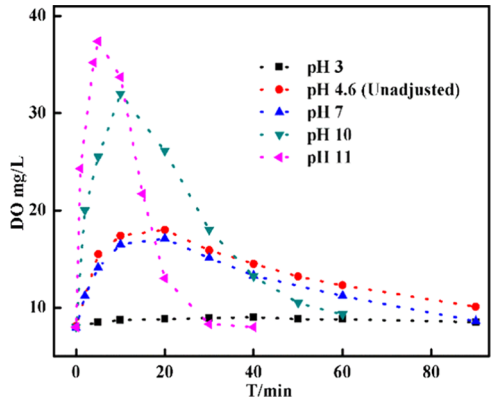

Figure 6. Change in dissolved oxygen in the presence of 2 g/L CDs/g-C_3N_4/Cu_xO with time under different pH conditions with the initial concentration of $[H_2O_2]_0$ = 10 mM, $[Rh\ B]_0$ = 0.064 mM, and V = 100 mL.

and then decreases. The maximum was obtained earlier with higher pH. The reason can be explained as follows: the experiment was carried out in the air, and according to Henry's law, the initial concentration of dissolved oxygen is 8 mg/L, and the observed increase in dissolved oxygen concentration is attributed to oxygen formation in the solution being faster than the equilibration with the surrounding gas phase. As the reaction ($H_2O_2 \rightarrow 1/2O_2+H_2O$) continues, the formation rate of O_2 increases sharply and is dependent on the pH.[53] With the consumption of H_2O_2, the formation of O_2 also slows down; thus, the peak appears. Such a trend and pH dependence are in line with the results in Figure 5.

2.2.5.3. Ion Leaching under Different pH Conditions. According to several studies, the leaching of copper ions from the present heterogeneous system may be affected by pH.[54,55] The concentration of dissolved Cu species was measured by inductively coupled plasma (ICP) spectrometry in the presence of a typical heterogeneous system (Figure 7). It can be seen that higher pH inhibits Cu leaching; the maximum concentration at pH 3 was about 60 times that at pH 11. According to the Eh-pH diagram of Cu-H_2O,[29,56,57] it mainly exists in the form of Cu^{2+} or Cu^{+}, and Cu_2O and $Cu(OH)_2$ under acidic and alkali conditions, respectively. It was observed that the leaching of copper ions on the catalyst surface was promoted under acidic

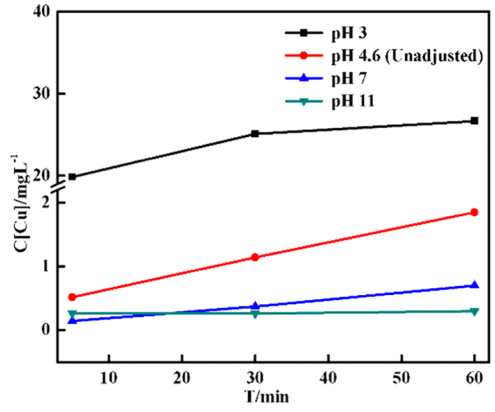

Figure 7. Change in the total copper ion concentration in the presence of 2 g/L CDs/g-C_3N_4/Cu_xO with time under different pH conditions with the initial concentration of $[H_2O_2]_0$ = 5 mM, $[Rh\ B]_0$ = 0.064 mM, and V = 100 mL.

conditions; it had a certain inhibitory effect on the leaching of ions on the catalyst surface under alkaline conditions, thereby indicating that the surface reaction of the composite was dominant in the reaction.

2.2.5.4. Recycling Experiment. To verify the recyclability and stability of the prepared CDs/g-C_3N_4/Cu_xO composite, three sets of recycling experiments were explored. In the wet cycle, the number of composites remains unchanged, and Rh B and H_2O_2 were directly added after the reaction. In the dry cycle, a series of centrifugation, washing, and drying treatments were used on the composites after the reaction for the next cycle reaction. The composites were recycled via a wet or dry process, and the pH was fixed at 11, 4.6, and 10.

2.2.5.4.1 *Recycling via the Wet Process at pH 11* The first set was performed at pH 11 via a wet recycling process since the original degradation rate of Rh B is relatively high. The concentrations of both H_2O_2 and Rh B against reaction time were investigated during each cycle (Figure S9). The decomposition rate of H_2O_2 slightly declined after 12 continuous cycles, while the degradation ratio of Rh B declined dramatically from 88.8 to 67.5% (Figure S9a). Then, Rh B was cyclically degraded under the same conditions (Figure S9b). The time interval was 30 min, and Rh B and H_2O_2 were added at the end of each cycle. It was noticed that although Rh B can be efficiently degraded by the CDs/g-C_3N_4/Cu_xO composites, the degradation efficiency is reduced after 10 cycles with incomplete degradation. The H_2O_2 concentration was adjusted from 5 to 10 mM under pH 11, and H_2O_2 showed rapid decomposition completely (Figure S10). In addition to the influence of method error and the side reaction at pH 11, it was observed that the degradation residues cover the surface of the composites for the wet cycle, thereby affecting the progress of the reaction.

2.2.5.4.2. *Recycling via the Dry Process at pH 4.6 (Unadjusted pH)* To reduce the impact of pH adjustment, under unadjusted pH (as the catalytic degradation performance is not lower than that under some pH conditions), a dry method was used to evaluate the circulation performance of CDs/g-C_3N_4/Cu_xO. As shown in Figure S11, the degradation of Rh B and the consumption of H_2O_2 are significantly affected by the number of cycles, and both experience a significant decrease. This indicates that the dry process has a greater impact on the CDs/g-C_3N_4/Cu_xO composite. At pH 4.6, the copper on the surface of the CDs/g-C_3N_4/Cu_xO composite mainly exists in the form of ions on the solution and causes loss of copper on the surface of the composite during the dry process.

2.2.5.4.3. *Recycling via the Dry Process at pH 10 Conditions* After optimizing the conditions, combined with the influence of pH 10, the CDs/g-C_3N_4/Cu_xO composite has a higher degradation efficiency for Rh B, so the dry method is also used to study the circulation performance of CDs/g-C_3N_4/Cu_xO. After eight cycles, the degradation efficiency of the composite on Rh B could be reduced by 4%, and the degradation ratio reached more than 95% in each cycle (Figure 8b). At the same time, the H_2O_2 consumed in each cycle was tested, and it almost completely decomposed after eight cycles, as shown in Figure 8a. This is because at pH 10, the copper on the surface of the composite mainly exists in the form of Cu_2O and $Cu(OH)_2$, and the loss of copper ions during the dry process can be overlooked. This observation agrees with the previous results regarding the ion leaching shown in Figure 7.

Therefore, it can be concluded that the CDs/g-C_3N_4/Cu_xO composite has good stability and strong catalytic performance at pH 10. To further establish the stability of the material, the XRD

https://dx.doi.org/10.1021/acsomega.0c05915
ACS Omega 2021, 6, 8119−8130

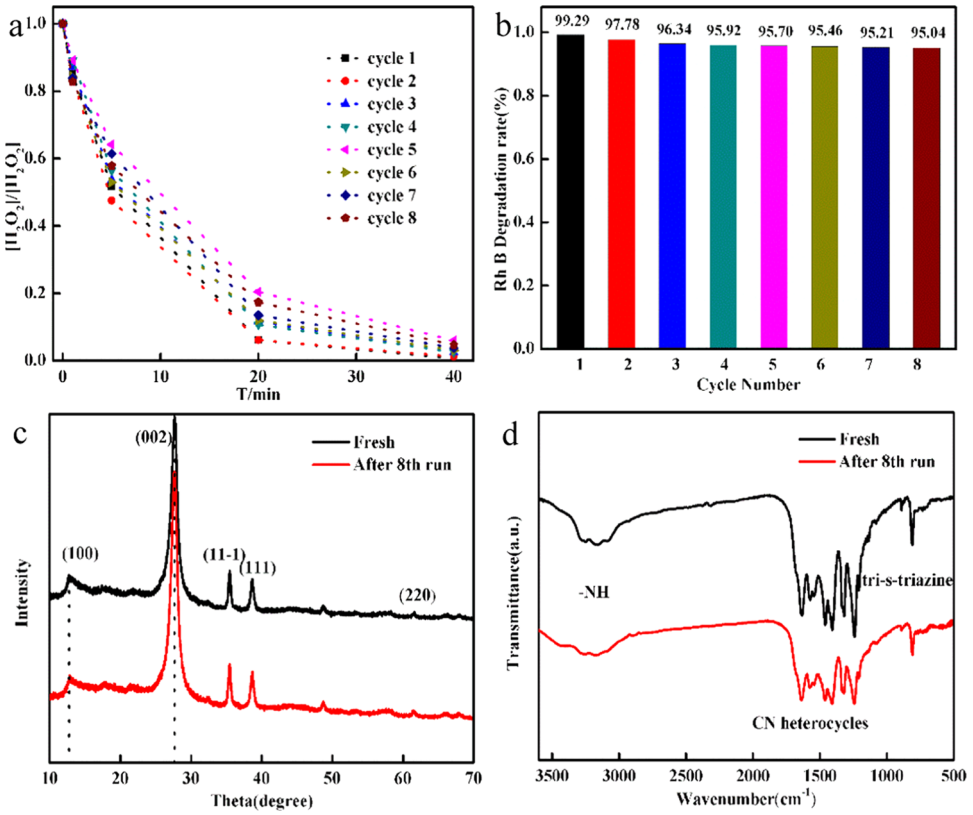

Figure 8. (a) Cyclic degradation of Rh B consumed and the change of H_2O_2 with 2 g/L CDs/g-C_3N_4/Cu_xO composite in the presence of 10 mM H_2O_2 at pH 10. (b) Cycling runs for the catalytic degradation of Rh B (0.064 mM) with 2 g/L CDs/g-C_3N_4/Cu_xO composite in the presence of 10 mM H_2O_2 at pH 10. (c) XRD patterns and (d) FT-IR spectra of the CDs/g-C_3N_4/Cu_xO sample before and after the cycling catalytic experiments.

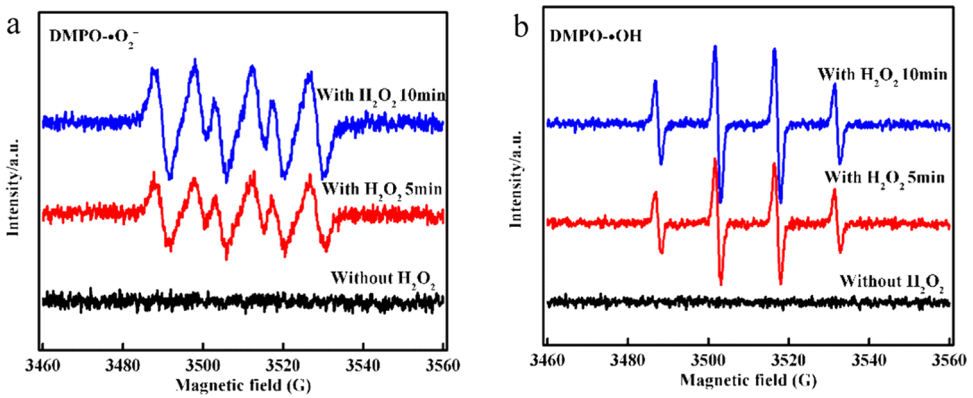

Figure 9. (a) DMPO spin-trapping EPR spectra of DMPO-$^{\bullet}O_2^-$ in methanol dispersion in the Rh B degradation experiment and (b) DMPO-$^{\bullet}$OH in aqueous dispersion in the Rh B degradation experiment with the CDs/g-C_3N_4/Cu_xO composite.

and FT-IR spectral patterns of the CDs/g-C_3N_4/Cu_xO composite were studied before and after the 8th reaction cycle (Figure 8c,d). No noticeable changes were seen after the reaction in the structure and elemental groups of CDs/g-C_3N_4/Cu_xO.

A comparison with the previous studies was made in terms of cycle stability and pH range to validate the catalytic performance of the prepared CDs/g-C_3N_4/Cu_xO composite. Better cycle stability and a wider range of pH applications were observed for the prepared composites (Table S3).[58−61] Therefore, the above findings show outstanding activity and reusability of the as-prepared CDs/g-C_3N_4/Cu_xO.

2.2.6. Degradation Mechanism. To determine the mechanism of Rh B degradation by the CDs/g-C_3N_4/Cu_xO composite at different pH conditions, radical trapping experiments and ESR analyses were designed and the main active species generated by Rh B degradation were identified.

2.2.6.1. Radical Trapping. Several studies have shown that P-benzoquinone (BQ) and isopropanol (IPA) are often used as scavengers for $^{\bullet}$OH and $^{\bullet}O_2^-$ because they can quickly trap free radicals (Table S4) and have a high reaction rate constant.[51,53,62] In particular, *p*-benzoquinone (BQ) was used as a scavenger for superoxide ($^{\bullet}O_2^-$) and hydroxyl radicals ($^{\bullet}$OH); isopropanol (IPA) may react with only $^{\bullet}$OH.[63] Additionally, pure N_2 purging was employed to investigate the effect of dissolved oxygen in the reaction. The degradation rate of Rh B retarded after the addition of IPA (10 mM) and BQ (10 mM), but it got suppressed more significantly with the addition of BQ since BQ

https://dx.doi.org/10.1021/acsomega.0c05915
ACS Omega 2021, 6, 8119−8130

can trap both $^{\bullet}OH$ and $^{\bullet}O_2^-$, while IPA only traps $^{\bullet}OH$ (Figure S12a). Moreover, the inhibition effect of IPA increases as its concentration increases. By comparing the results with and without N_2, it was observed that Rh B degradation is affected by the presence of O_2.

To determine the inhibition effect of the scavengers more clearly, the reaction parameters were fitted to a pseudo-first-order kinetic model, and the corresponding parameters are shown in Figure S12c (where k represents the reaction rate). It can be seen that the reaction is significantly inhibited after adding the scavengers and introducing N_2, and the fitting results are consistent with the results shown in Figure S12a. The results indicate that $^{\bullet}OH$ and $^{\bullet}O_2^-$ are the main oxidation species in the reaction process,[64] and O_2 has a certain positive effect on the reaction. However, neither scavenger nor O_2 affected the H_2O_2 decomposition (Figure S12b).

To further determine the effect of pH on the generation of free radicals, free radical capture experiments were carried out under the conditions of pH 4.6 and 10 (Figure S12d). As can be seen, BQ shows a better inhibition effect than that of IPA at a given pH, which means that $^{\bullet}O_2^-$ is more significant than $^{\bullet}OH$ on the degradation of Rh B or the production of $^{\bullet}O_2^-$ is higher than $^{\bullet}OH$. Moreover, by comparing the data after the addition of IPA or BQ with the blank at a certain pH, it is clear that the inhibition effect is also basic-favored.

The EPR experiment was conducted to further identify the existence of $^{\bullet}OH$ and $^{\bullet}O_2^-$, radicals formed during the reaction of the CDs/g-C_3N_4/Cu_xO composite. The spin-trapping DMPO (5,5-dimethyl-1-pyrroline-*N*-oxide) (100 mM) is a persistent radical scavenger to trap other radicals, such as DMPO-$^{\bullet}O_2^-$ or DMPO-$^{\bullet}OH$, which are spin adducts with characteristic EPR signals. The EPR signal was not clearly observed without the H_2O_2 condition (Figure 9a), whereas it clearly revealed a four-line spectrum with the relative intensities of 1:1:1:1 with H_2O_2, a characteristic signal of the DMPO-$^{\bullet}O_2^-$ adduct.[65] Besides, the EPR spectra featuring the characteristic 1:2:2:1 quartet indicated successful trapping of $^{\bullet}OH$ by DMPO with H_2O_2 in the Rh B degradation experiment as depicted in Figure 9b.[32] Further, no EPR signal of spin adduct DMPO-$^{\bullet}OH$ was observed without H_2O_2. The results are consistent with those of the trapping experiments. Hence, we further verified the dominant role of $^{\bullet}OH$ and $^{\bullet}O_2^-$ active species.

2.2.6.2. Mechanism. Based on the above-mentioned results, a mechanism was proposed (see Scheme 1). In the heterogeneous system containing the CDs/g-C_3N_4/Cu_xO composite, H_2O_2, and Rh B, there are acidic-favored solution reactions, basic-favored surface reactions, and pH-independent surface reactions, while the surface reactions dominate the degradation of Rh B.

Scheme 1. Mechanism of Various Radical Generations over CDs/g-C_3N_4/Cu_xO in a Catalytic System

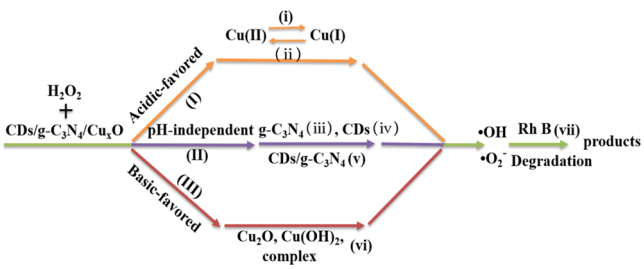

It can be said that under acidic conditions, dissolved Cu(I) is mainly generated in the reaction system and undergoes a homogenous Fenton-like reaction with H_2O_2 to produce $^{\bullet}OH$ and $^{\bullet}O_2^-$ in solution; the related process is presented in (i) and (ii) and denoted reaction (I).[30] However, under basic conditions, Cu_2O, $Cu(OH)_2$, and the complex mainly exist in the reaction system, which can react with H_2O_2 to produce $^{\bullet}OH$ and $^{\bullet}O_2^-$ radicals through surface reactions, mostly catalytic decomposition of H_2O_2, and the related reaction III is shown as (Vi).[56,57] Besides, H_2O_2 can be catalytically decomposed on the surface of CDs, g-C_3N_4, and the matrix of the CDs/g-C_3N_4/Cu_xO composite, generating $^{\bullet}OH$ and $^{\bullet}O_2^-$ (as per the related process presented as (iii), (iv), and (v)) (i.e., reaction II).[26,66,67] Since reaction (II) did not involve light exposure, it was relatively slow in this work, and the reactions are pH-independent.[57] Therefore, the major reactions in the heterogeneous system are reactions (I) and (II) in the acidic solution and reactions (II) and (III) in the basic solution. The role of reaction (I) is more significant under the acidic condition as compared to the basic condition (Figures 5 and S7). However, the major reactions in the heterogeneous system are the surface reactions (II) and (III) irrespective of the solution pH.

As compared to the acidic conditions, under basic conditions, the CDs/g-C_3N_4/Cu_xO composite exhibited stronger catalytic activity and stability, which can continuously decompose H_2O_2 to generate $^{\bullet}OH$ and $^{\bullet}O_2^-$ so as to induce Rh B degradation (Figures 5 and S9). Also, the curve of degradation of Rh B follows the decomposition trend of H_2O_2 with the same pH, thereby indicating that pH primarily affects the decomposition of H_2O_2 and thus the degradation of Rh B (Figure 5).

The $^{\bullet}OH$ and $^{\bullet}O_2^-$ produced in this reaction are used for the degradation of Rh B, and the related process is shown in (vii).[66] For the analysis of Rh B products, the degradation products after the reaction could be analyzed by LC/MS.[68] Generally, the decomposition of Rh B undergoes a three-step process: N-deethylation, chromophore cleavage with subsequent triazine ring-opening, and mineralization.[69] The active free radicals produced by the reaction destroy the structure of Rh B, degrading it into less harmful compounds.

3. CONCLUSIONS

In this work, a catalyst CDs/g-C_3N_4/Cu_xO was synthesized by a simple homogeneous method of thermal polymerization with stepwise modification of g-C_3N_4 with CDs and Cu_2O, the catalytic performance of which is strongly pH-dependent. The major findings are enumerated as follows.

- In the applied pH range (3−11), the catalytic performance is increased by raising the solution pH (45−96%). The optimal pH was confirmed to be 10 due to the relatively high degradation ratio of Rh B, lower consumption of H_2O_2, and better recyclability.
- The dry method in the recycling experiments shows better recyclability than using the wet method. The degradation ratio of Rh B, in the dry method at pH 10, remains 95% even after eight cycles.
- The major reactive species leading to the Rh B degradation in the present system are confirmed to be $^{\bullet}OH$ and $^{\bullet}O_2^-$.
- In the proposed mechanism, the major reactions in the heterogeneous system are reactions (I) and (II) in the acidic solution, and the role of reaction (I) is more significant, while the major reactions are reactions (II)

https://dx.doi.org/10.1021/acsomega.0c05915
ACS Omega 2021, 6, 8119−8130

and (III) in the basic solution, which are mainly the surface reactions in the heterogeneous system.

Overall, in this study, we developed a promising Fenton-like catalyst that exhibits a wider working pH and good recyclability and overcomes the narrow workable pH of the Fenton reaction.

4. EXPERIMENTAL SECTION

4.1. Reagents. Reagents used in this study included melamine (CP, $C_3H_6N_6$, ≥99.0%), citric acid monohydrate (AR, $C_6H_8O_7{\cdot}H_2O$, ≥99.5%), cuprous oxide (AR, Cu_2O, ≥97.0%), hydrogen peroxide (CP, H_2O_2, 30.0%), acetic acid (AR, CH_3COOH, ≥99.5%), sodium acetate (AR, $CH_3COONa{\cdot}3H_2O$, ≥99.5%), potassium iodide (AR, KI, ≥99.0%), ammonium molybdate (CP, $H_8MoN_2O_4$, 56.5%), ethanol (AR, C_2H_6O, 99.7%), hydrochloric acid (AR, HCl, 36%), sodium hydroxide (AR, NaOH, ≥98.0%), isopropanol (AR, IPA, ≥99.7%), *p*-benzoquinone (CP, BQ, ≥98.0%), rhodamine B (AR, $C_{28}H_{31}ClN_2O_3$, ≥99.0%), 5,5-dimethyl-1-pyrroline-*N*-oxide (AR, DMPO, ≥97.0%), and nitrogen (CP, N_2, ≥99.0%) stored in gas cylinders. All solutions were prepared with deionized water, and all chemicals were supplied by the manufacturer (Sinopharm Chemical Reagent co. Ltd., Shanghai, China) and used as received without further purification.

4.2. Preparation of CDs/g-C_3N_4/Cu_xO Composites. *4.2.1. CDs/g-C_3N_4.* CDs/g-C_3N_4 composites were prepared by thermal polymerization, using citric acid monohydrate as the precursor of CDs as previously reported.[70] Typically, 0.6 g of citric acid and 20 g of melamine were placed in an aluminum crucible, mixed well, and calcined at 600 °C for 3 h at the ramping rate of 2 °C min^{-1} in a muffle furnace. After naturally cooling down at room temperature (RT), the CD_3/g-C_3N_4 composite was obtained. Furthermore, several CD_y/g-C_3N_4 composites (*y*, 1−6) that included different amounts of CDs were prepared, where y represents the initial mass ratio of citric acid monohydrate to melamine.

4.2.2. CDs/g-C_3N_4/Cu_xO Composite. The cuprous oxide (Cu_2O)-modified CDs/g-C_3N_4 composite was prepared by a similar thermal polymerization pathway as previously reported.[71] Typically, 5 g of CDs/g-C_3N_4 composite material and 0.14 g of Cu_2O were added to 10 mL of ethanol solution with stirring for 0.5 h. The mixed material/solution was placed in an aluminum crucible, heated at a ramp of 1 °C min^{-1} to 520 °C for 3 h, and cooled to RT in a muffle furnace. The derived powder was stored and labeled as C2. Additionally, CDs/g-C_3N_4/Cu_xO composites that included different amounts of Cu_2O were prepared (Table S5).

4.3. Material Characterization. Fourier transform infrared spectroscopy (Nicolet iS5 FT-IR spectrometer, Thermo Fisher Scientific) was used to investigate the samples of infrared absorption spectra using the standard potassium bromide (KBr) disk method in the wavenumber range from 400 to 4000 cm^{-1}.

The structural properties of the composite were detected by powder X-ray diffraction (XRD, D/max- III A, Bruker Corporation, Germany) measurements, which used Cu Kα radiation (λ = 1.54 Å; angle of 2θ, 10−70°).

The morphology and microstructure of the synthesized composites were characterized by transmission electron microscopy (TEM) (TEM JEM-2100 model, JEOL Ltd., Japan) and high-resolution TEM (HRTEM).

An investigation of the surface component elemental state of the resultant catalyst was done using X-ray photoelectron spectroscopy (XPS, via an ESCALAB 250XI, Thermo Fisher Scientific, Inc.), and the C 1s signal at 284.60 eV was used as the internal standard to calibrate binding energies.

The specific surface and pore volume were analyzed by the Brunauer−Emmett−Teller (BET) (TriStar II 3020, Micromeritics Instrument Corporation, Georgia) via isothermal desorption and adsorption with high-purity nitrogen.

The absorbance of the studied reagents, i.e., H_2O_2 and Rh B, was measured by a V-5600 spectrophotometer (Shanghai Metash Instruments Co. Ltd., China) and a UV-5500 PC (Shanghai Metash Instruments Co. Ltd., China) spectrophotometer in the wavelength range of 200−800 nm.

The pH of the solutions was measured using the ST2100 pH meter (China) with an accuracy of ±0.01 pH units and a working temperature from 5 to 40 °C.

The prepared samples were weighed to $\pm 10^{-4}$ g in an ME104E microbalance (Mettler Toledo, China).

The dissolved oxygen (DO) of the solution was analyzed by the portable dissolved oxygen meter (JPB-607A, China).

An inductively coupled plasma optical emission spectrometer (ICP-OES) Prodigy 7 (Teledyne instrument Labs, Mason, OH) was used to measure the total copper ion concentration of the solution.

The ROS were detected by electron paramagnetic resonance (EPR) using an A300 spectrometer (Bruker Instrument, Germany) and spin-trapping agents such as 5,5-dimethyl-1-pyrrolidine-*N*-oxide (DMPO, 100 mM) aqueous solution (Bruker Instrument, Germany).

4.4. Catalytic Activity Experiment. Rh B was used as the target dye for evaluating the catalytic properties of the synthesized composites. All catalytic degradation experiments were conducted in the dark with magnetic stirring at RT.

In a typical experiment, a certain amount of synthesized composite was added to the Rh B solution and stirred for 40 min to achieve adsorption/desorption equilibrium before the addition of H_2O_2, which triggered the catalysis. At fixed time points, 4 mL of suspension was taken and filtered using a 0.22 μm membrane filter. The absorbance was measured so as to obtain the time-resolved concentrations of H_2O_2 and Rh B. In some cases, the concentrations of H_2O_2, Rh B, and dissolved copper species in the filtered samples were also monitored to evaluate the potential reaction in the homogeneous system.

The concentration of Rh B was determined by measuring the absorbance at 555 nm using an ultraviolet−visible (UV−vis) spectrophotometer. The H_2O_2 concentration was detected by the Ghormley triiodide method, which states that I^- could be oxidized to triiodide (I_3^-) by H_2O_2 in the presence of acetic acid and the catalyst ammonium molybdate (AMD). The absorbance of I_3^- can be measured by a spectrophotometer at 350 nm.[72] The intermediate products produced in the experiment may interfere with the measurements, but the experimental error was less than 2% for the concentrations of Rh B and H_2O_2 determined.

The specific free radical scavengers, including benzoquinone (BQ) and isopropanol (IPA), were separately added into the suspension after the adsorption−desorption equilibrium before the addition of H_2O_2, scavenging $^{\bullet}O_2^-$ and $^{\bullet}OH$, respectively.[73] Additionally, the suspension was purged with N_2 to remove O_2 in the whole reaction process.

The degree of degradation was expressed by degradation ratios and utilization, which are defined in eqs 3 and 4,[74] where $[\text{Rh B}]_0$ or $[H_2O_2]_0$ is the initial concentration of Rh B and H_2O_2, and $[\text{Rh B}]_t$ or $[H_2O_2]_t$ is the concentration of Rh B (mM) or H_2O_2 at time *t* (*t* = 60 min), respectively. All of these

https://dx.doi.org/10.1021/acsomega.0c05915
ACS Omega 2021, 6, 8119−8130

experiments were carried out in beakers in the dark to avoid dye sensitization.

$$\text{degradation ratios } \% = \frac{[\text{RhB}]_0 - [\text{RhB}]_t}{[\text{RhB}]_0} \times 100\% \quad (3)$$

$$\text{utilization } \% = \frac{[\text{RhB}]_0 - [\text{RhB}]_t}{[\text{H}_2\text{O}_2]_0 - [\text{H}_2\text{O}_2]_t} \times 100\% \quad (4)$$

■ ASSOCIATED CONTENT

Supporting Information

The Supporting Information is available free of charge at https://pubs.acs.org/doi/10.1021/acsomega.0c05915.

FT-IR spectra of g-C_3N_4, CD_3/g-C_3N_4, and CDs/g-C_3N_4/Cu_xO composites (Figure S1); XRD patterns of Cu_2O, g-C_3N_4, CD_3/g-C_3N_4, and CDs/g-C_3N_4/Cu_xO composites (Figure S2); XPS spectra of the CDs/g-C_3N_4/Cu_xO composite (Figure S3); high-resolution XPS spectra of O 1s (Figure S4); N_2 adsorption/desorption isotherm and the pore-size distribution of g-C_3N_4, CD_3/g-C_3N_4,and CDs/g-C_3N_4/Cu_xO (Figure S5); $[\text{Rh B}]/[\text{Rh B}]_0$ as a function of time with different H_2O_2 concentrations in the presence of 2 g/L CDs/g-C_3N_4/Cu_xO composite with the initial concentration of $[\text{Rh B}]_0$ = 0.064 mM and V = 100 mL (Figure S6); $[\text{Rh B}]/[\text{Rh B}]_0$ as a function of time in stock CDs/g-C_3N_4/Cu_xO (2 g/L) suspensions and filtrates obtained at selected time intervals with the initial concentration of $[\text{Rh B}]_0$ = 0.064 mM, $[H_2O_2]_0$ = 5 mM, and V = 100 mL; degradation of Rh B in heterogeneous catalytic reaction and filtered solution in 1 min reacting over a longer period of time (Figure S7); variation of the Rh B wavelength at different pH values (Figure S8); recycling performance for 5 mM H_2O_2 decomposition in the presence of the 2 g/L CDs/g-C_3N_4/Cu_xO composite at pH 11 at 25 min per cycle and V = 100 mL; recycling performance of the 2 g/L CDs/g-C_3N_4/Cu_xO composite for Rh B (0.064 mM) degradation in the presence of 5 mM H_2O_2 at pH 11 at 30 min per cycle (Figure S9); $[\text{Rh B}]/[\text{Rh B}]_0$ as a function of time in the presence of the 2 g/L CDs/g-C_3N_4/Cu_xO composite for Rh B (0.064 mM) degradation in the presence of 10 mM H_2O_2 at pH 11 (Figure S10); H_2O_2 consumed in cycling reactions by the 2 g/L CDs/g-C_3N_4/Cu_xO composite for Rh B (0.064 mM) degradation in the presence of 5 mM H_2O_2 at pH 4.6 (unadjusted pH; V = 100 mL); recycling degradation of the Rh B (0.064 mM) was conducted by the 2 g/L CDs/g-C_3N_4/Cu_xO composite in the presence of 5 mM H_2O_2 at pH 4.6 (unadjusted pH; V = 100 mL) (Figure S11); $[\text{Rh B}]/[\text{Rh B}]_0$ and $[H_2O_2]/[H_2O_2]_0$ as a function of time in the presence of different quenchers by the 2 g/L CDs/g-C_3N_4/Cu_xO composite for Rh B (0.064 mM) degradation in the presence of 5 mM H_2O_2; parameters of the pseudo-first-order kinetic models of different quenchers by the 2 g/L CDs/g-C_3N_4/Cu_xO composite for Rh B (0.064 mM) degradation in the presence of 5 mM H_2O_2; $[\text{Rh B}]/[\text{Rh B}]_0$ as a function of time in the presence of different quenchers by the 2 g/L CDs/g-C_3N_4/Cu_xO composite for Rh B (0.064 mM) degradation in the presence of 5 mM H_2O_2 at different pH values (Figure S12); XPS results of the CDs/g-C_3N_4/Cu_xO composite (Table S1); efficiency of Rh B at different H_2O_2 concentrations (Table S2); comparison of the catalytic performance of CDs/g-C_3N_4/Cu_xO and several reported relative studies (Table S3); reaction formulas and reaction rate constants of possible reactions in radical trapping (Table S4); and the initial mass ratio of Cu_2O to CDs/g-C_3N_4 for CDs/g-C_3N_4/Cu_xO composites (Table S5) (PDF)

■ AUTHOR INFORMATION

Corresponding Author

Miao Yang − *School of Chemistry, Chemical Engineering and Life Sciences, Wuhan University of Technology, Wuhan 430070, China;* orcid.org/0000-0003-4522-772X; Email: yangmiao@whut.edu.cn

Authors

Yulian Guo − *School of Chemistry, Chemical Engineering and Life Sciences, Wuhan University of Technology, Wuhan 430070, China*

Chunsun Zhou − *School of Chemistry, Chemical Engineering and Life Sciences, Wuhan University of Technology, Wuhan 430070, China*

Lijuan Fang − *School of Chemistry, Chemical Engineering and Life Sciences, Wuhan University of Technology, Wuhan 430070, China*

Zhongda Liu − *School of Chemistry, Chemical Engineering and Life Sciences, Wuhan University of Technology, Wuhan 430070, China*

Wen Li − *School of Chemistry, Chemical Engineering and Life Sciences, Wuhan University of Technology, Wuhan 430070, China*

Complete contact information is available at: https://pubs.acs.org/10.1021/acsomega.0c05915

Notes

The authors declare no competing financial interest.

■ ACKNOWLEDGMENTS

This research was financially supported by the National Natural Science Foundation of China (217071108) and the Fundamental Research Funds for the Central Universities (WUT: 2018IVB044).

■ REFERENCES

(1) Gui, L.; Peng, J.; Li, P.; Peng, R.; Yu, P.; Luo, Y. Electrochemical degradation of dye on TiO_2 nanotube array constructed anode. *Chemosphere* **2019**, *235*, 1189−1196.

(2) Phanichphant, S.; Nakaruk, A.; Channei, D. Photocatalytic activity of the binary composite CeO_2/SiO_2 for degradation of dye. *Appl. Surf. Sci.* **2016**, *387*, 214−220.

(3) Zhao, Q.; Mao, Q.; Zhou, Y.; Wei, J.; Liu, X.; Yang, J.; Luo, L.; Zhang, J.; Chen, H.; Chen, H.; et al. Metal-free carbon materials-catalyzed sulfate radical-based advanced oxidation processes: A review on heterogeneous catalysts and applications. *Chemosphere* **2017**, *189*, 224−238.

(4) An, T.; Yang, H.; Li, G.; Song, W.; Nie, X.; et al. Kinetics and mechanism of advanced oxidation processes (AOPs) in degradation of ciprofloxacin in water. *Appl. Catal., B* **2010**, *94*, 288−294.

(5) Bilińska, L.; Gmurek, M.; Ledakowicz, S. Textile wastewater treatment by AOPs for brine reuse. *Process Saf. Environ. Prot.* **2017**, *109*, 420−428.

(6) Petrat, F.; Paluch, S.; Dogruoz, E.; Dorfler, P.; Kirsch, M.; Korth, H. G.; Sustmann, R.; De Groot, H. Reduction of Fe(III) ions complexed to physiological ligands by lipoyl dehydrogenase and other flavoenzymes in vitro: implications for an enzymatic reduction of

Fe(III) ions of the labile iron pool. *J. Biol. Chem.* **2003**, *278*, 46403−46413.
(7) Mousavi, M.; Habibi-Yangjeh, A.; Pouran, S. R. Review on magnetically separable graphitic carbon nitride-based nanocomposites as promising visible-light-driven photocatalysts. *J. Mater. Sci.: Mater. Electron.* **2018**, *29*, 1719−1747.
(8) Eshaq, G.; ElMetwally, A. E. Bmim[OAc]-Cu_2O/g-C_3N_4 as a multi-function catalyst for sonophotocatalytic degradation of methylene blue. *Ultrason. Sonochem.* **2019**, *53*, 99−109.
(9) Zhao, H.; Wang, Y.; Wang, Y.; Cao, T.; Zhao, G. Electro-Fenton oxidation of pesticides with a novel Fe_3O_4@Fe_2O_3/activated carbon aerogel cathode: High activity, wide pH range and catalytic mechanism. *Appl. Catal., B* **2012**, *125*, 120−127.
(10) Chen, F.; Xie, S.; Huang, X.; Qiu, X. Ionothermal synthesis of Fe_3O_4 magnetic nanoparticles as efficient heterogeneous Fenton-like catalysts for degradation of organic pollutants with H_2O_2. *J. Hazard. Mater.* **2017**, *322*, 152−162.
(11) Liu, X.; Wu, X.; Long, Z.; Zhang, C.; Ma, Y.; Hao, X.; Zhang, H.; Pan, C. Photodegradation of Imidacloprid in Aqueous Solution by the Metal-Free Catalyst Graphitic Carbon Nitride using an Energy-Saving Lamp. *J. Agric. Food. Chem.* **2015**, *63*, 4754−4760.
(12) Zhang, H.; Zhao, L.; Geng, F.; Guo, L.-H.; Wan, B.; Yang, Y. Carbon dots decorated graphitic carbon nitride as an efficient metal-free photocatalyst for phenol degradation. *Appl. Catal., B* **2016**, *180*, 656−662.
(13) Fang, S.; Xia, Y.; Lv, K.; Li, Q.; Jie, S.; Mei, L. Effect of carbon-dots modification on the structure and photocatalytic activity of g-C_3N_4. *Appl. Catal., B* **2016**, *185*, 225−232.
(14) Bai, X.; Wang, L.; Wang, Y.; Yao, W.; Zhu, Y. Enhanced oxidation ability of g-C_3N_4 photocatalyst via C60 modification. *Appl. Catal., B* **2014**, *152*−*153*, 262−270.
(15) Zhao, H.; Wang, J.; Dong, Y.; Jiang, P. Noble-Metal-Free Iron Phosphide Cocatalyst Loaded Graphitic Carbon Nitride as an Efficient and Robust Photocatalyst for Hydrogen Evolution under Visible Light Irradiation. *ACS Sustainable Chem. Eng.* **2017**, *5*, 8053−8060.
(16) Fang, S.; Xia, Y.; Lv, K.; Li, Q.; Sun, J.; Li, M. Effect of carbon-dots modification on the structure and photocatalytic activity of g-C_3N_4. *Appl. Catal., B* **2016**, *185*, 225−232.
(17) Ellis, J. E.; Sorescu, D. C.; Burkert, S. C.; White, D. L.; Star, A. Uncondensed Graphitic Carbon Nitride on Reduced Graphene Oxide for Oxygen Sensing via a Photoredox Mechanism. *ACS Appl. Mater. Interfaces* **2017**, *9*, 27142−27151.
(18) Ma, J.; Yang, Q.; Wen, Y.; Liu, W. Fe-g-C_3N_4/graphitized mesoporous carbon composite as an effective Fenton-like catalyst in a wide pH range. *Appl. Catal., B* **2017**, *201*, 232−240.
(19) Li, D.; Zan, J.; Wu, L.; Zuo, S.; Xu, H.; Xia, D. Heterojunction Tuning and Catalytic Efficiency of g-C_3N_4-Cu_2O with Glutamate. *Ind. Eng. Chem. Res.* **2019**, *58*, 4000−4009.
(20) Sano, T.; Tsutsui, S.; Koike, K.; Hirakawa, T.; Teramoto, Y.; Negishi, N.; Takeuchi, K. Activation of graphitic carbon nitride (g-C_3N_4) by alkaline hydrothermal treatment for photocatalytic NO oxidation in gas phase. *J. Mater. Chem. A* **2013**, *1*, 6489−6496.
(21) Akhundi, A.; García-López, E. I.; Marcì, G.; Habibi-Yangjeh, A.; Palmisano, L. Comparison between preparative methodologies of nanostructured carbon nitride and their use as selective photocatalysts in water suspension. *Res. Chem. Intermed.* **2017**, *43*, 5153−5158.
(22) Liu, J.; Liu, Y.; Liu, N.; Han, Y.; Zhang, X.; Huang, H.; Lifshitz, Y.; Lee, S. T.; Zhong, J.; Kang, Z. Metal-free efficient photocatalyst for stable visible water splitting via a two-electron pathway. *Science* **2015**, *347*, 970−974.
(23) Li, Y.; Feng, X.; Lu, Z.; Yin, H.; Liu, F.; Xiang, Q. Enhanced photocatalytic H_2-production activity of C-dots modified g-C_3N_4/TiO_2 nanosheets composites. *J. Colloid Interface Sci.* **2018**, *513*, 866−876.
(24) Miao, X.; Yue, X.; Ji, Z.; Shen, X.; Zhou, H.; Liu, M.; Xu, K.; Zhu, J.; Zhu, G.; Kong, L.; et al. Nitrogen-doped carbon dots decorated on g-C_3N_4/Ag_3PO_4 photocatalyst with improved visible light photocatalytic activity and mechanism insight. *Appl. Catal., B* **2018**, *227*, 459−469.
(25) Dadigala, R.; Bandi, R.; Gangapuram, B. R.; Guttena, V. Carbon dots and Ag nanoparticles decorated g-C_3N_4 nanosheets for enhanced organic pollutants degradation under sunlight irradiation. *J. Photochem. Photobiol., A* **2017**, *342*, 42−52.
(26) Liu, Z.; Shen, Q.; Zhou, C.; Fang, L.; Yang, M.; Xia, T. Kinetic and Mechanistic Study on Catalytic Decomposition of Hydrogen Peroxide on Carbon-Nanodots/Graphitic Carbon Nitride Composite. *Catalysts.* **2018**, *8*, 445.
(27) Guo, F.; Shi, W.; Guan, W.; Huang, H.; Liu, Y. Carbon dots/g-C_3N_4/ZnO nanocomposite as efficient visible-light driven photocatalyst for tetracycline total degradation. *Sep. Purif. Technol.* **2017**, *173*, 295−303.
(28) Sun, B.; Li, H.; Li, X.; Liu, X.; Zhang, C.; Xu, H.; Zhao, X. S. Degradation of Organic Dyes over Fenton-Like Cu_2O-Cu/C Catalysts. *Ind. Eng. Chem. Res.* **2018**, *57*, 14011−14021.
(29) Zhou, C.; Liu, Z.; Fang, L.; Guo, Y.; Feng, Y.; Yang, M. Kinetic and Mechanistic Study of Rhodamine B Degradation by H_2O_2 and Cu/Al_2O_3/g-C_3N_4 Composite. *Catalysts* **2020**, *10*, No. 317.
(30) Xu, S.; Zhu, H.; Cao, W.; Wen, Z.; Wang, J.; François-Xavier Philippe, C.; Wintgens, T. Cu-Al_2O_3-g-C_3N_4 and Cu-Al_2O_3-C-dots with dual-reaction centres for simultaneous enhancement of Fenton-like catalytic activity and selective H_2O_2 conversion to hydroxyl radicals. *Appl. Catal., B* **2018**, *234*, 223−233.
(31) Liu, B.; Wu, Y.; Zhang, J.; Han, X.; Shi, H. Visible-light-driven g-C_3N_4/Cu_2O heterostructures with efficient photocatalytic activities for tetracycline degradation and microbial inactivation. *J. Photochem. Photobiol., A* **2019**, *378*, 1−8.
(32) Chang, P.-Y.; Tseng, I.-H. Photocatalytic conversion of gas phase carbon dioxide by graphitic carbon nitride decorated with cuprous oxide with various morphologies. *J. CO_2 Util.* **2018**, *26*, 511−521.
(33) Asadzadeh-Khaneghah, S.; Habibi-Yangjeh, A.; Yubuta, K. Novel g-C_3N_4 nanosheets/CDs/BiOCl photocatalysts with exceptional activity under visible light. *J. Am. Ceram. Soc.* **2019**, *102*, 1435−1453.
(34) Peng, B.; Zhang, S.; Yang, S.; Wang, H.; Yu, H.; Zhang, S.; Peng, F. Synthesis and characterization of g-C_3N_4/Cu_2O composite catalyst with enhanced photocatalytic activity under visible light irradiation. *Mater. Res. Bull.* **2014**, *56*, 19−24.
(35) Li, D.; Zan, J.; Wu, L.; Zuo, S.; Xu, H.; Xia, D. Heterojunction Tuning and Catalytic Efficiency of g-C_3N_4-Cu_2O with Glutamate. *Ind. Eng. Chem. Res.* **2019**, *58*, 4000−4009.
(36) Li, D.; Zuo, S.; Xu, H.; Zan, J.; Sun, L.; Han, D.; Liao, W.; Zhang, B.; Xia, D. Synthesis of a g-C_3N_4-Cu_2O heterojunction with enhanced visible light photocatalytic activity by PEG. *J. Colloid Interface Sci.* **2018**, *531*, 28−36.
(37) Chen, X.; Kuo, D. H.; Lu, D. F. Nanonization of g-C_3N_4 with the assistance of activated carbon for improved visible light photocatalysis. *RSC Adv.* **2016**, *6*, 66814−66821.
(38) Xu, S.; Zhu, H.; Cao, W.; Wen, Z.; Wang, J.; François-Xavier Philippe, C.; Wintgens, T. Cu-Al_2O_3-g-C_3N_4 and Cu-Al_2O_3-C-dots with dual-reaction centres for simultaneous enhancement of Fenton-like catalytic activity and selective H_2O_2 conversion to hydroxyl radicals. *Appl. Catal., B* **2018**, *234*, 223−233.
(39) Sahu, K.; Bisht, A.; Kuriakose, S.; Mohapatra, S. Two-dimensional CuO-ZnO nanohybrids with enhanced photocatalytic performance for removal of pollutants. *J. Phys. Chem. Solids* **2020**, *137*, No. 109223.
(40) Zuo, S.; Xu, H.; Liao, W.; Yuan, X.; Sun, L.; Li, Q.; Zan, J.; Li, D.; Xia, D. Molten-salt synthesis of g-C_3N_4-Cu_2O heterojunctions with highly enhanced photocatalytic performance. *Colloids Surf., A.* **2018**, *546*, 307−315.
(41) Fang, S.; Yang, X.; Kangle, L.; Qin, L.; Jie, S. B.; et al. Effect of carbon-dots modification on the structure and photocatalytic activity of g-C_3N_4. *Appl. Catal., B.* **2016**, *185*, 225−232.
(42) Fang, S.; Xia, Y.; Lv, K.; Li, Q.; Sun, J.; Li, M. Effect of carbon-dots modification on the structure and photocatalytic activity of g-C_3N_4. *Appl. Catal., B.* **2016**, *185*, 225−232.
(43) Min, Z.; Wang, X.; Li, Y.; Jiang, J.; Li, J.; Qian, D.; Li, J. A highly efficient visible-light-responding Cu_2O-TiO_2/g-C_3N_4 photocatalyst for instantaneous discolorations of organic dyes. *Mater. Lett.* **2017**, *193*, 18−21.

https://dx.doi.org/10.1021/acsomega.0c05915
ACS Omega 2021, 6, 8119−8130

(44) Sareen, S.; Mutreja, V.; Singh, S.; Pal, B. Highly dispersed Au, Ag and Cu nanoparticles in mesoporous SBA-15 for highly selective catalytic reduction of nitroaromatics. *RSC Adv.* **2015**, *5*, 184−190.
(45) Ma, X.; Zhang, J.; Wang, B.; Li, Q.; Chu, S. Hierarchical Cu_2O foam/g-C_3N_4 photocathode for photoelectrochemical hydrogen production. *Appl. Surf. Sci.* **2018**, *427*, 907−916.
(46) Ji, C.; Yin, S.-N.; Sun, S.; Yang, S. An in situ mediator-free route to fabricate Cu_2O/g-C_3N_4 type-II heterojunctions for enhanced visible-light photocatalytic H_2 generation. *Appl. Surf. Sci.* **2018**, *434*, 1224−1231.
(47) Zuo, S.; Haiming, X.; Wei, L.; Xiangjuan, Y.; Lei, S.; Qiang, L.; Jie, Z.; Dongya, L.; Xia, D. Molten-salt synthesis of g-C_3N_4-Cu_2O heterojunctions with highly enhanced photocatalytic performance. *Colloids Surf., A* **2018**, *546*, 307−305.
(48) Thaweesak, S.; Wang, S.; Lyu, M.; Xiao, M.; Peerakiatkhajohn, P.; Wang, L. Boron-doped graphitic carbon nitride nanosheets for enhanced visible light photocatalytic water splitting. *Dalton Trans.* **2017**, *46*, 10714−10720.
(49) Kavitha, V.; Palanivelu, K. Destruction of cresols by Fenton oxidation process. *Water Res.* **2005**, *39*, 3062−3072.
(50) Zhang, S.; Gao, H.; Huang, Y.; Wang, X.; Hayat, T.; Li, J.; Xu, X.; Wang, X. Ultrathin g-C_3N_4 nanosheets coupled with amorphous Cu-doped FeOOH nanoclusters as 2D/0D heterogeneous catalysts for water remediation. *Environ. Sci.: Nano* **2018**, *5*, 1179−1190.
(51) Fang, L.; Liu, Z.; Zhou, C.; Guo, Y.; Feng, Y.; Yang, M. Degradation Mechanism of Methylene Blue by H_2O_2 and Synthesized Carbon Nanodots/Graphitic Carbon Nitride/Fe(II) Composite. *J. Phys. Chem. C* **2019**, *123*, 26921−26931.
(52) Yang, M.; Jonsson, M. Evaluation of the O_2 and pH Effects on Probes for Surface Bound Hydroxyl Radicals. *J. Phys. Chem. C* **2014**, *118*, 7971−7979.
(53) Babuponnusami, A.; Muthukumar, K. A review on Fenton and improvements to the Fenton process for wastewater treatment. *J. Environ. Chem. Eng.* **2014**, *2*, 557−572.
(54) Ma, Q.-B.; Hofmann, J. P.; Litke, A.; Hensen, E. J. M. Cu_2O photoelectrodes for solar water splitting: Tuning photoelectrochemical performance by controlled faceting. *Sol. Energy Mater. Sol. Cells* **2015**, *141*, 178−186.
(55) Zhou, H.; Kang, L.; Zhou, M.; Zhong, Z.; Xing, W. Membrane enhanced COD degradation of pulp wastewater using Cu_2O/H_2O_2 heterogeneous Fenton process. *Chin. J. Chem. Eng.* **2018**, *26*, 1896−1903.
(56) Ma, Q.-B.; Hofmann, J. P.; Litke, A.; Hensen, E. J. M. Cu_2O photoelectrodes for solar water splitting: Tuning photoelectrochemical performance by controlled faceting. *Sol. Energy Mater. Sol. Cells* **2015**, *141*, 178−186.
(57) Aylmore, M. G.; Muir, D. M. Thermodynamic analysis of gold leaching by ammoniacal thiosulfate using Eh/pH and speciation diagrams. *Min., Metall., Explor.* **2001**, *18*, 221−227.
(58) Chen, T.; Zhu, Z.; Zhang, H.; Shen, X.; Qiu, Y.; Yin, D. Enhanced Removal of Veterinary Antibiotic Florfenicol by a Cu-Based Fenton-like Catalyst with Wide pH Adaptability and High Efficiency. *ACS Omega* **2019**, *4*, 1982−1994.
(59) Lyu, L.; Han, M.; Cao, W.; Gao, Y.; Zeng, Q.; Yu, G.; Huang, X.; Hu, C. Efficient Fenton-like process for organic pollutant degradation on Cu-doped mesoporous polyimide nanocomposites. *Environ. Sci.: Nano* **2019**, *6*, 798−808.
(60) Nekoeinia, M.; Yousefinejad, S.; Hasanpour, F.; Yousefian-Dezaki, M. Highly efficient catalytic degradation of p-nitrophenol by Mn_3O_4.CuO nanocomposite as a heterogeneous fenton-like catalyst. *J. Exp. Nanosci.* **2020**, *15*, 322−336.
(61) Zhang, Y.; Liu, C.; Xu, B.; Qi, F.; Chu, W. Degradation of benzotriazole by a novel Fenton-like reaction with mesoporous Cu/MnO_2: Combination of adsorption and catalysis oxidation. *Appl. Catal., B* **2016**, *199*, 447−457.
(62) Watts, R. J.; Teel, A. L. Hydroxyl radical and non-hydroxyl radical pathways for trichloroethylene and perchloroethylene degradation in catalyzed H_2O_2 propagation systems. *Water Res.* **2019**, *159*, 46−54.
(63) Rodríguez, E. M.; Márquez, G.; Tena, M.; Álvarez, P. M.; Beltrán, F. J. Determination of main species involved in the first steps of TiO_2 photocatalytic degradation of organics with the use of scavengers: The case of ofloxacin. *Appl. Catal., B* **2015**, *178*, 44−53.
(64) Dong, G.; Ai, Z.; Zhang, L. Total aerobic destruction of azo contaminants with nanoscale zero-valent copper at neutral pH: promotion effect of in-situ generated carbon center radicals. *Water Res.* **2014**, *66*, 22−30.
(65) Lu, H.; Liu, X.; Liu, F.; Hao, Z.; Zhang, J.; Lin, Z.; Barnett, Y.; Pan, G. Visible-light photocatalysis accelerates As(III) release and oxidation from arsenic-containing sludge. *Appl. Catal., B* **2019**, *250*, 1−9.
(66) Wang, X.; Li, D.; Nan, Z. Effect of N content in g-C_3N_4 as metal-free catalyst on H_2O_2 decomposition for MB degradation. *Sep. Purif. Technol.* **2019**, *224*, 152−162.
(67) Zhu, Q.; Liu, G.; Yan, M.; Ye, J.; Zhu, L.; Huang, J.; Yang, X. Cu(2+) enhanced chemiluminescence of carbon dots-H_2O_2 system in alkaline solution. *Talanta* **2020**, *208*, No. 120380.
(68) He, Z.; Yang, S.; Ju, Y.; Sun, C. Microwave photocatalytic degradation of Rhodamine B using TiO_2 supported on activated carbon: Mechanism implication. *Global J. Environ. Sci.* **2009**, *21*, 268−272.
(69) Fatima, R.; Kim, J.-O. Inhibiting photocatalytic electron-hole recombination by coupling MIL-125(Ti) with chemically reduced, nitrogen-containing graphene oxide. *Appl. Surf. Sci.* **2021**, *541*, No. 148503.
(70) Datta, A.; Kapri, S.; Bhattacharyya, S. Carbon dots with tunable concentrations of trapped anti oxidant as an efficient metal-free catalyst for electrochemical water oxidation. *J. Mater. Chem. A* **2016**, *4*, 14614−14624.
(71) Chen, J.; Shen, S.; Guo, P.; Wang, M.; Wu, P.; Wang, X.; Guo, L. In-situ reduction synthesis of nano-sized Cu_2O particles modifying g-C_3N_4 for enhanced photocatalytic hydrogen production. *Appl. Catal., B* **2014**, *152*−*153*, 335−341.
(72) Yang, M.; Zhang, X.; Grosjean, A.; Soroka, I.; Jonsson, M. Kinetics and Mechanism of the Reaction between H_2O_2 and Tungsten Powder in Water. *J. Phys. Chem. C* **2015**, *119*, 22560−22569.
(73) Liu, Q.; Guo, Y.; Chen, Z.; Zhang, Z.; Fang, X. Constructing a novel ternary Fe(III)/graphene/g-C_3N_4 composite photocatalyst with enhanced visible-light driven photocatalytic activity via interfacial charge transfer effect. *Appl. Catal., B* **2016**, *183*, 231−241.
(74) Fang, L.; Liu, Z.; Zhou, C.; Guo, Y.; Feng, Y.; Yang, M. Degradation Mechanism of Methylene Blue by H_2O_2 and Synthesized Carbon Nanodots/Graphitic Carbon Nitride/Fe(II) Composite. *J. Phys. Chem. C* **2019**, *123*, 26921−26931.

https://dx.doi.org/10.1021/acsomega.0c05915
ACS Omega 2021, 6, 8119−8130